

# Lawrence Berkeley National Laboratory

## LBL Publications

### Title

Aluminum/SmCo5 composites for structural and magnetic applications

### Permalink

<https://escholarship.org/uc/item/4t90z5gh>

### Journal

Journal of Materials Science, 59(36)

### ISSN

0022-2461

### Authors

Ishrak, Farhan

Lastovich, Michael

Malakar, Aniruddha

et al.

### Publication Date

2024-09-01

### DOI

10.1007/s10853-024-10208-3

### Copyright Information


This work is made available under the terms of a Creative Commons Attribution-NonCommercial-NoDerivatives License, available at

<https://creativecommons.org/licenses/by-nc-nd/4.0/>

Peer reviewed



# Aluminum/SmCo<sub>5</sub> composites for structural and magnetic applications

Farhan Ishrak<sup>1</sup>, Michael Lastovich<sup>1</sup>, Aniruddha Malakar<sup>1</sup>, Ravi Sankar Haridas<sup>2</sup>, Arun J. Bhattacharjee<sup>3,4</sup>, Huimin Qiao<sup>1</sup>, Matthew Clary<sup>1</sup>, Joseph Tracy<sup>1</sup>, Nina Balke<sup>1</sup>, Harrison P. Lisabeth<sup>3,4</sup>, Rajiv Mishra<sup>5</sup>, Mert Efe<sup>6</sup>, and Bharat Gwalani<sup>1,\*</sup> 

<sup>1</sup> Department of Materials Science and Engineering, North Carolina State University, Raleigh, NC 27695, USA

<sup>2</sup> Department of Mechanical Engineering, University of North Texas, Denton, TX 76203, USA

<sup>3</sup> Advanced Light Source, Lawrence Berkeley National Laboratory, Berkeley, CA 94720, USA

<sup>4</sup> Lawrence Berkeley National Laboratory, Energy Geosciences Division, Berkeley, CA 94720, USA

<sup>5</sup> Department of Materials Science and Engineering, University of North Texas, Denton, TX 76203, USA

<sup>6</sup> Energy and Environment Directorate, Pacific Northwest National Laboratory, Richland, WA 99352, USA

**Received:** 23 July 2024

**Accepted:** 5 September 2024

**Published online:**

14 September 2024

© The Author(s), under exclusive licence to Springer Science+Business Media, LLC, part of Springer Nature, 2024

## ABSTRACT

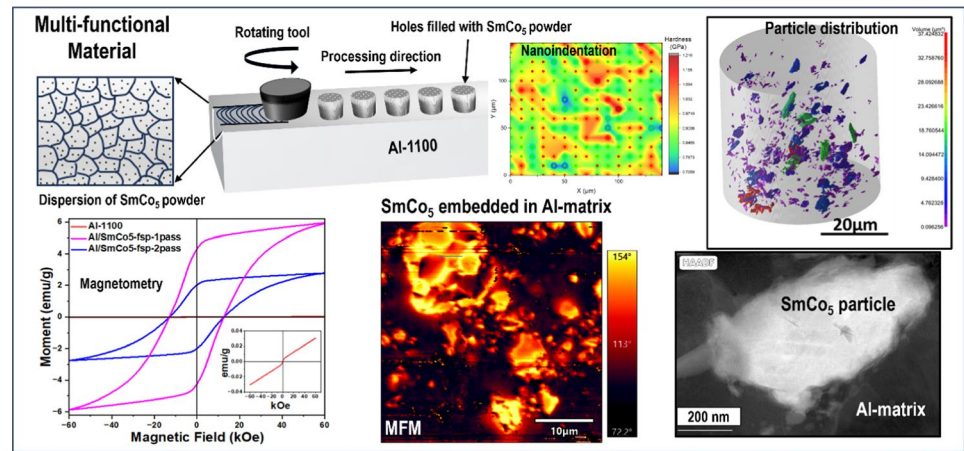
Metal-bonded magnetic composites (MBMCs) present a promising alternative to dense sintered magnets, particularly for intricate components. Compared to polymer-based bonded magnets, MBMCs have wider applicability in harsh environments. In this paper, we demonstrate a solid-state shear-based manufacturing technique to introduce localized magnetization into a paramagnetic aluminum matrix by embedding SmCo<sub>5</sub> permanent magnet particles. Our magnetic composites display hard magnetic behavior with a coercivity of 13 kOe and a remanent magnetization of 4.32 emu/g. In addition to magnetization, we also report a 9% improvement in Young's modulus. Despite the local temperature rise during processing, the magnetic phases didn't decompose into unwanted phases, preserving the composite's hard magnetic properties. Creation of an interfacial metallurgical bond with the matrix ensured the suitability of the composites for structural applications. Our study investigates the mechanical, and functional properties of composites, paving the way for lightweight structural magnetic composites with a transformative potential in the aerospace, nuclear, and automotive applications. This work underscores the potential for further optimization and development to drive innovations in magnet and equipment design.

Handling Editor: Peiyao Zhao.

Address correspondence to E-mail: bgwalan@ncsu.edu

<https://doi.org/10.1007/s10853-024-10208-3>

## GRAPHICAL ABSTRACT



## Introduction

Bonded magnets, comprised of a non-magnetic binder and magnetic powder, offer a compelling solution to the processing constraints encountered with fully dense sintered permanent magnets, particularly in microactuators and sensors [1, 2]. They offer a cost-effective and simpler manufacturing solution, particularly for intricate-shaped components. However, their predominantly polymer-based composition presents a formidable obstacle to their application in extreme environments characterized by elevated temperatures, mechanical stress, radiation exposure, and dynamic conditions [3]. This limitation underscores the pressing need to develop lightweight structural magnetic materials, whose transformative potential in aerospace, nuclear, and automotive applications remains largely unrealized. Enhancing the strength and toughness of magnetic materials holds significant potential for expanding their application in extreme conditions, such as in nuclear reactors, power plants, and space environments. Furthermore, these magnetic materials with graded magnetic susceptibility could lead to innovative designs for motors and transformers.

Magnetic composites based on metal matrices can be used in place of bonded magnets for more challenging environments such as reactor cores operating at elevated temperatures. Al alloys are widely used as a structural material in the automotive, aerospace, construction, medical devices, and household applications due to suitable mechanical strength, lightweight, wear and corrosion resistance, and recyclability [4–6]. With

a density of  $2.7 \text{ g/cm}^3$ —approximately one-third that of steel or Cu–Al alloys offer exceptional strength-to-weight ratios, making them indispensable in aerospace and automotive industries. Moreover, Al's corrosion resistance in diverse environments and moderate melting point ease composite processing. Pure Al, however, is paramagnetic and has poor magnetic properties, accordingly. Various joining mechanisms are employed for permanent magnets to attach with structural components such as soldering, adhesive bonding, and spot-welding, which hinder reliability and weight reduction, and increase the associated cost [7]. To mitigate this problem, we utilized solid state-based friction stir processing (FSP) [8, 9] to locally introduce permanent magnetic properties in a structural component. FSP, initially invented as a welding technique [10], can be used for developing composite materials by the addition of second-phase particles into a base substrate without drastically modifying the constituent phase structures [9].

In the past, several attempts have been made to incorporate magnetic powders in a metal matrix to make magnetic composites. Various soft metal (Zn, Sn, In, Al, Cu) bonded NdFeB, SmCo<sub>5</sub>, and SmFeN permanent magnets have been prepared using squeeze casting, microwave sintering, and powder metallurgy-based techniques such as rotary forging [11–16]. For example, Brett et al. investigated rotary-forged Al-matrix NdFeB composite, which exhibited a notable coercivity of 14 kOe. However, they observed a decline in magnetic properties when attempting to enhance the magnet's strength

through heat treatment [15]. Chuang et al. employed the squeeze casting method to prepare Al-bonded NdFeB magnets. The resulting magnets exhibited poor mechanical properties, in addition to deterioration of the magnetic phase caused by an unavoidable reaction with the aluminum due to the high processing temperature of 750 °C, significantly higher than its melting point [16]. On the other hand, ferromagnetic nanoparticles such as  $\text{Fe}_3\text{O}_4$ ,  $\text{CoFe}_2\text{O}_4$ , and  $\text{NiFe}_2\text{O}_4$  have been embedded into an Al matrix to produce a metal matrix composite [17–20]. However, none of these efforts have aimed to produce site-specific permanent magnetic composite suitable for structural applications. Maleki et al. synthesized Al matrix composites containing magnetic nickel ferrite nanoparticles, which exhibited a negligible coercivity of 121 Oe [18]. Borgohain et al. reported a saturation magnetization of 17.07 emu/g for Al reinforced with 10 wt% cobalt ferrite, but the process resulted in a very low coercivity of 0.5 kOe [20]. Mahmoud et al. produced an Al-based magnetic surface composite using Fe and  $\text{Fe}_3\text{O}_4$  magnetite powders by FSP which showed soft magnetic behavior and interfacial reactions between Fe particles and Al-matrix yielding poor magnetic properties [21]. Our current work is targeted towards unlocking a new class of magnetic composites by utilizing a strong permanent magnet to bond with or embed in a metal matrix. This work demonstrates the ability to produce localized hard magnetic composites. Additionally, this study indicates that an increase in the fraction of magnetic powders and optimization of processing parameters can concurrently increase the functional properties by several folds.

In this study, we used FSP to embed  $\text{SmCo}_5$  magnetic powder particles in commercially available paramagnetic aluminum alloys.  $\text{SmCo}_5$  demonstrates an exceptionally high maximum energy product ( $\text{BH}_{\text{max}}$ ), even surpassing neodymium magnets particularly when operating at elevated temperatures [22]. It shows superior radiation resistance to demagnetization when compared with the NdFeB magnets [23]. Moreover, it offers significantly greater plasticity through the formation of shear bands, which can enhance its suitability for deformation processing applications [24–26]. We investigated the mechanical and functional properties of the processed alloy with multi-modal characterization measurements.

## Experimental

The study utilized a 6 mm thick, and 50 mm wide rolled plate of commercial AA 1100 aluminum purchased from McMaster-Carr with a nominal composition as the base material. Two sets of five consecutive holes 2.3 mm in diameter, 3 mm deep, and 5.25 mm apart were drilled into the Al plate using a Tormach 440 PCNC machine.  $\text{SmCo}_5$  powder (purchased from American Elements) was then used to fill the holes. Each hole contained approximately 100 mg of the powder which was 11.13 by wt.% or 3.6 by vol.%, as shown in the schematic (Fig. 1a1). FSP was performed on both sets of filled holes using a Manufacturing Technology Inc. friction stir welding machine at the center for friction stir processing (CFSP) at the University of North Texas. An AISI H13 (ASTM A681) steel tool head with a conical pin (shoulder diameter of 15 mm, pin root diameter of 6 mm, and pin depth of 4 mm) was employed. The tool rotated at 350 RPM and traversed at a rate of 150 mm/min with a 2.5° tool tilt.

A second FSP pass was conducted specifically on the second set of filled holes. For this pass, the tool rotation speed remained at 350 RPM, while the traverse speed was increased to 200 mm/min. Samples were sectioned using a slow-speed saw with a diamond wafering blade from the center of the stir zone and then compression-mounted in phenolic using Buehler SimpliMet 4000. The samples were ground up to 1200 grit, using emery papers, and then polished up to a 0.02  $\mu\text{m}$  finish, using a colloidal silica on a manual metallurgical polishing wheel.

Initial microstructural characterization of the polished sample was performed using a Hitachi SU3900 scanning electron microscope (SEM). Electron backscatter diffraction (EBSD) of the microstructure was performed using a Helios Hydra G5 fitted with Hikari Super EBSD at an operating voltage of 15 kV. Apex suite and TSL OIM 8 software were used for EBSD data acquisition and analysis, respectively. The EBSD specimens were prepared after polishing down to 1200 grit and vibratory polishing for 3 h. X-ray diffraction (XRD) was performed at room temperature on a Rigaku Smartlab X-ray diffractometer using a standard Bragg–Brentano geometry with  $\text{Cu K}\alpha$  radiation ( $\lambda = 1.54 \text{ \AA}$ , 40 kV, 44 mA) to identify the phases present in the processed sample. X-ray microtomography was performed at the 8.3.2. microCT beamline at the advanced light source, Lawrence Berkeley National Laboratory, using a 25 keV monochromatic beam to



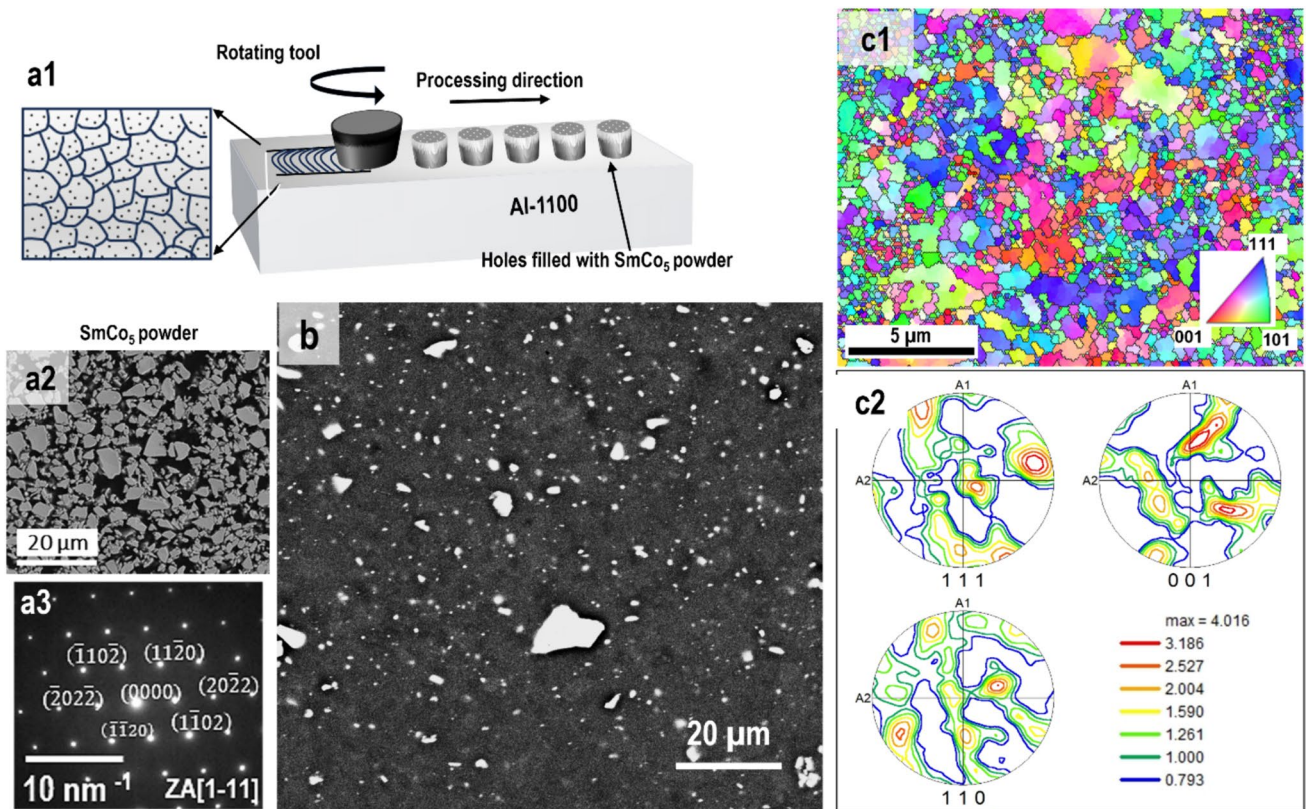


**Figure 1** **a1** Schematic showing the operational setup of the FSP process where an H13 steel tool rotates at 350 RPM and 2.5° tilt locally stirs the Al matrix along with the magnetic powder inside the drilled holes to homogenize and refine the as-cast microstructure. The bar was processed one time at a traverse speed of 150 mm/min for the full bar length and then a second pass was done at 200 mm/min for part of the first passed region. Magnified

schematic from the stir zone shows the fine grain microstructure and the dispersion of SmCo<sub>5</sub> powders in the Al matrix; **a2** BSE image of SmCo<sub>5</sub> magnetic powders; **a3** SAED pattern of SmCo<sub>5</sub> powders; **b** high magnification image showing the fine-scale distribution of the SmCo<sub>5</sub> particles in the FSPed region; **c** EBSD data (**c1**) inverse pole figure (IPF) map from the FSPed region (**c2**) corresponding pole figure.

acquire 1500 projections of each sample over 180° sample rotation. X-ray nanotomography was performed at the 11.3.1 tender X-ray beamline at the advanced light source, Lawrence Berkeley National Laboratory, using a 7 keV monochromatic beam to acquire 512 projections of each sample over 180° sample rotation. Reconstruction of the micro- and nanoCT data was performed using the NERSC supercomputer with the help of a modified reconstruction code based on Tomopy [27]. 3D visualization of the data and volumetric measurements was performed using dragonfly ORS. Samples were prepared for transmission electron microscopy (TEM) using the standard lift-out procedure on an FEI thermo scientific quanta 3D Ga<sup>+</sup> focused ion beam (FIB) system. The TEM foils were characterized by scanning transmission electron microscopy (STEM) and energy-dispersive X-ray spectroscopy (EDS),

selected area electron diffraction (SAED), and electron energy loss spectroscopy (EELS). A quantum design MPMS 3 superconducting quantum interference device vibrating sample magnetometer (SQUID-VSM) was used for magnetometry. The magnetic moment (*M*) was measured at room temperature with respect to the applied magnetic field (*H*) up to 60 kOe to plot the *M*–*H* loop at a scan rate of 200 Oe/s. Magnetic force microscopy (MFM) was employed to observe the distribution of magnetic domains and grains in the bulk Al matrix after processing. MFM was performed with a multimode atomic force microscope (MFP-3D Infinity, Asylum Research, U.S.). A *n* + silicon tip with resistivity of 0.01–0.02 Ωcm, height of 10–15 micron and hard magnetic coating from Nanosensors was used. A scan speed of 0.5 Hz and a set point of 0.7 V were used with 256 lines per scan direction. Before MFM

measurement, the tip (MFMR, NanoWorld) was magnetized by placing it on a permanent magnet. MFM data was analyzed using the open-source gwyddion software.

Nanomechanical testing was performed using the Hysitron (Bruker) TI 980 triboindenter, equipped with a diamond Berkovich indenter tip. To prepare for nanoindentation, samples were polished using a 0.02  $\mu\text{m}$  colloidal silica solution to achieve a mirror finish, ensuring that surface roughness would not affect the indentation process. Nanohardness ( $H$ ) and Young's (reduced) modulus ( $E_r$ ) were determined using the Oliver–Pharr analytical method [28]. Nanoindentation mapping was conducted with a single cycle load-controlled indentation protocol, where a 6 mN load was applied at 10  $\mu\text{m}$  intervals between a total of 225 indents. This process involved a 5 s linear load to the maximum force, a 2 s hold, and a subsequent 5 s linear unload. The accuracy of the indentation measurements was confirmed by calibrating the indenter tip geometry on a fused quartz standard with known hardness and reduced modulus values.

## Results and discussions

Figure 1a1 shows a schematic of the surface modification process via FSP. The temperature evolution during processing was estimated using the model established by Arbegast and Hartley for Al alloys [29]. This relationship, represented as

$$\frac{T}{T_m} = K \left( \frac{w^2}{V \cdot 10^4} \right)^\alpha$$

where  $T$  represents the maximum temperature during processing;  $T_m$  is the alloy melting point;  $w$  is the rotation speed in RPM;  $V$  indicates the traverse speed in mm/min; and  $K$  represents the scale factor. For Al alloys, the range of  $K$  lies between 0.65 and 0.75, while the exponent  $\alpha$  varies from 0.04 to 0.06. Using this model, the processing temperature was determined to be around 350–400  $^\circ\text{C}$ . This temperature is well below the melting point of Al, facilitating microstructure refinement and the distribution of second-phase  $\text{SmCo}_5$  particles during solid-phase processing.

Characterization of the as-received magnetic powders (Fig. 1a2) reveals the particles to have a broad size distribution,  $31 \pm 11 \mu\text{m}$ , and irregular morphologies. Electron diffraction (Fig. 1a3) confirms the powders

to be single-phase  $\text{SmCo}_5$ , with no observable secondary phases. After incorporation into the Al plate via FSP, these particles are seen to inhabit extended channels within the microstructure, heterogeneously distributed within the metal matrix. While the phase fraction of particles was homogenized in the stir zone, the size distribution of  $\text{SmCo}_5$  particles remained heterogeneous even after a second pass of the tool which was done for homogenization and redistribution. After the second, a bimodal size distribution arises between the larger particles ( $\sim 17 \mu\text{m}$ ) in these channels and within the inter-channel regions ( $\sim 5 \mu\text{m}$ ), both likely reduced from the original size through particle fracture brought on by the intense plastic shear of the rotating FSP tool. The SEM shows a high magnification view in Fig. 1b, revealing the submicron  $\text{SmCo}_5$  particles dispersed within fine-grained Al-matrix. The irregular shapes of  $\text{SmCo}_5$  further support a severe plastic deformation-induced fragmentation of these particles.

EBSD on a double-pass processed Al/ $\text{SmCo}_5$  composite (Fig. 1c1) shows that a combination of high shear strain and frictional heating during FSP resulted in microstructural refinement, ultimately producing randomly oriented grains  $\sim 730 \pm 500 \text{ nm}$  in size. The plastic deformation experienced at elevated temperatures during FSP created conducive conditions for dynamic recrystallization (DRX) phenomena [30]. This DRX, as discussed by Cavaliere, is driven by the significant thermal energy produced by the tool during processing [31].

Pole figures (Fig. 1c2) illustrate the presence of shear texture components, including  $B/\bar{B}$ ,  $A_1^*/A_2^*$ , and  $A/\bar{A}$ , with the  $A_1^*/A_2^*$  component being less prominent. The formation of the B partial fiber involves continuous lattice rotations, aligning the  $\{112\}$  plane parallel to the shear plane and the  $\langle 110 \rangle$  direction with the shear direction. Similarly, alignment for the A partial fiber occurs with the  $\{111\}$  plane parallel to the shear plane and the  $\langle 112 \rangle$  direction aligned with the shear direction. The observed texture evolution closely resembles that documented during the FSP of Al alloys [32, 33]. The presence of shear texture components indicates that the microstructural evolution occurred via a continuous dynamic recrystallization process (CDRX) [32, 34]. However, it was previously suggested that in the presence of reinforcement particles, the microstructure evolution during FSP might proceed via the particle-stimulated nucleation (PSN) process [35]. During FSP,



fine reinforcement particles can impede dislocation movement and serve as nucleation sites for recrystallization leading to PSN. This phenomenon results in the formation of randomly oriented recrystallized grains surrounding the particles, ultimately reducing the overall texture intensity. Therefore, the microstructure is refined by a combination of CDRX, which produces the shear texture, and PSN, which similarly refines the structure while softening the texture components.

SEM-EDS results in Fig. 2a1–a4 confirm that the particles are  $\text{SmCo}_5$  intermetallic after processing within the double-pass processed alloy, revealing their dispersion occurred during tool-induced mechanical stirring. Two distinct-sized populations of  $\text{SmCo}_5$  generated by particle fracture retain the original magnetic phase. XRD analysis was conducted to identify the phases within the Al-bonded  $\text{SmCo}_5$  magnetic composite, with measurements performed at room temperature. In Fig. 2b, XRD traces from the

Al/ $\text{SmCo}_5$  composite (after 2 passes) display reflections corresponding to the face-centered cubic (FCC) Al alloy, along with visible peaks diffracted from the (101), (110), (111), and (112) planes of the  $\text{SmCo}_5$  particles. While a small fraction of the magnetic phase is present in the processed region, the absence of additional identifiable phases in the X-ray pattern indicates unwanted reactions were adequately suppressed during processing.

To get an average particle distribution, X-ray tomography was used, analyzing both single-pass and double-pass samples. Figure 2c1 and d1 demonstrates a higher particle number density in the double-pass sample compared to the single-pass counterpart, with 1484 particles per  $\text{mm}^3$  in the single pass and 25,307 particles per  $\text{mm}^3$  in the double pass. Furthermore, nanoCT data (Fig. 2c2 and d2) reveals that particles are smaller in size when FSP is conducted in multiple passes. The double-pass specimen shows

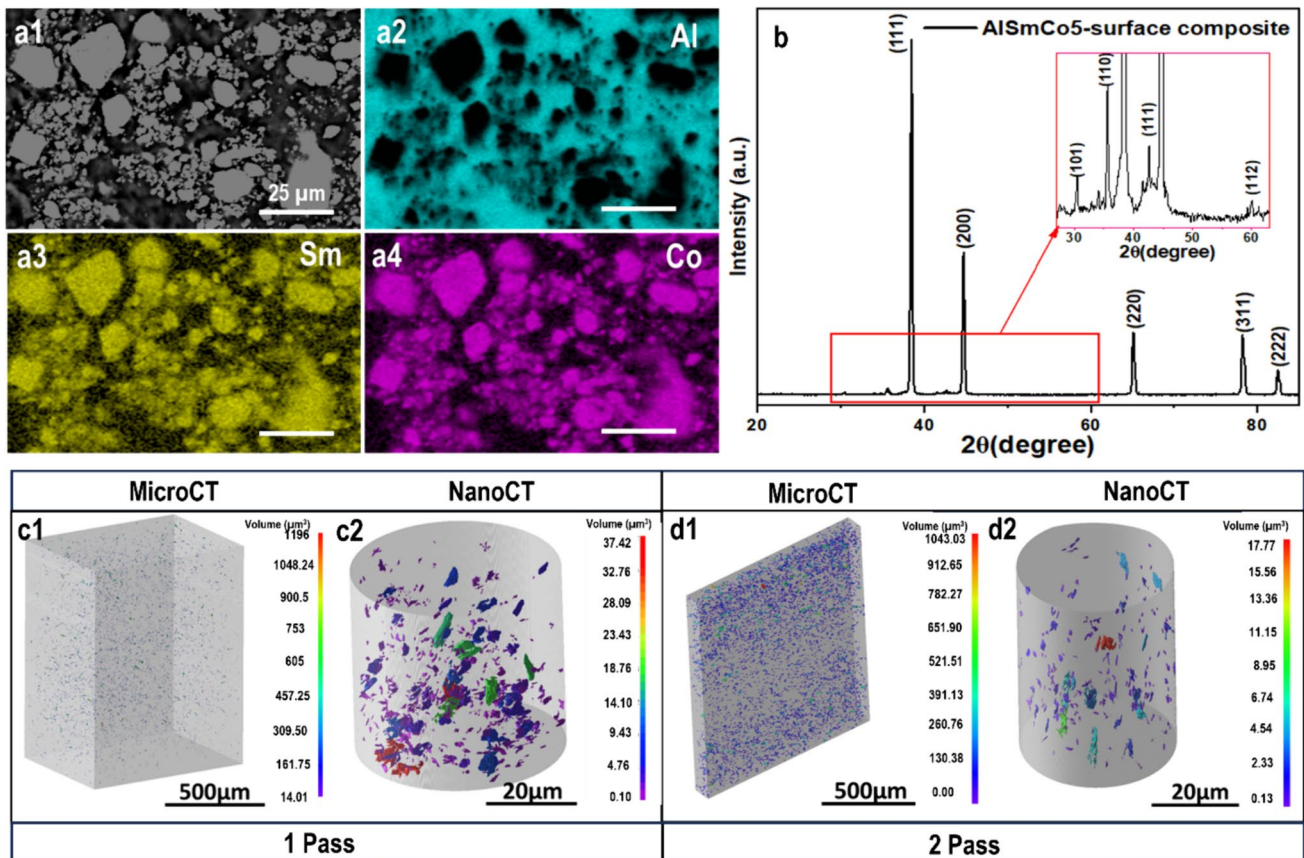


**Figure 2** a1–a4 SEM-EDS of the double-pass FSPed region showing the bimodal distribution of particle size in the top view of the processed region (high particle density region); b X-ray patterns of the processed region which shows characteristic peaks

of  $\text{SmCo}_5$  along with FCC phase of Al matrix; X-ray micro- and nanotomography analysis for c1 and c2 single-pass and d1 and d2 double-pass friction stir processed composites.

predominantly broken particles, with some appearing elongated before fracture. The breaking and dispersion result in a lower volume fraction of magnetic particles in the matrix after two passes which has direct consequences on magnetic properties (shared in detail in Fig. 3). Previous studies have demonstrated that increasing the number of FSP passes from one to four leads to uniform dispersion of nano-sized  $\text{Al}_2\text{O}_3$  particles, a six-fold decrease in average  $\text{Al}_2\text{O}_3$  cluster size, and a reduction in the grain size of the Al matrix [36]. Due to the better distribution and breakage of  $\text{SmCo}_5$  particles achieved through double-pass FSP, further details are focused on the double-pass sample.

To evaluate the overall magnetic response of the processed sample, magnetometry was conducted on the processed sample, previously characterized in Fig. 2a1–a4. In Fig. 3a, magnetization ( $M$ ) measurements at room temperature are depicted against the applied magnetic field ( $H$ ) up to 60 kOe for the unprocessed Al alloy and both the single and double-pass

processed Al-matrix magnetic composite. The pure Al alloy demonstrates paramagnetic behavior without a hysteresis loop (see Fig. 3a inset). Conversely, processing the Al bar with  $\text{SmCo}_5$  magnetic powders yields a magnetic composite with hard magnetic behavior. The Al/ $\text{SmCo}_5$  composite demonstrates an intrinsic coercivity of  $\sim 12.88$  kOe after a single pass and  $\sim 13.01$  kOe after the double pass. The remanent magnetization is 4.32 emu/g for the single pass and 2.02 emu/g for the double pass. The decrease in remanent magnetization after the first pass could be a direct consequence of the reduction in the magnetic portion in the matrix per unit volume due to centrifugal dispersion. The notable coercivity observed in this composite can be attributed to the significant particle fragmentation during FSP, as reducing particle size is known to enhance the coercivity of  $\text{SmCo}_5$  [37]. It is also assumed that the magnetic properties of the  $\text{SmCo}_5$  phase were maintained during processing, and no magnetic exchange effects from the Al were observed.

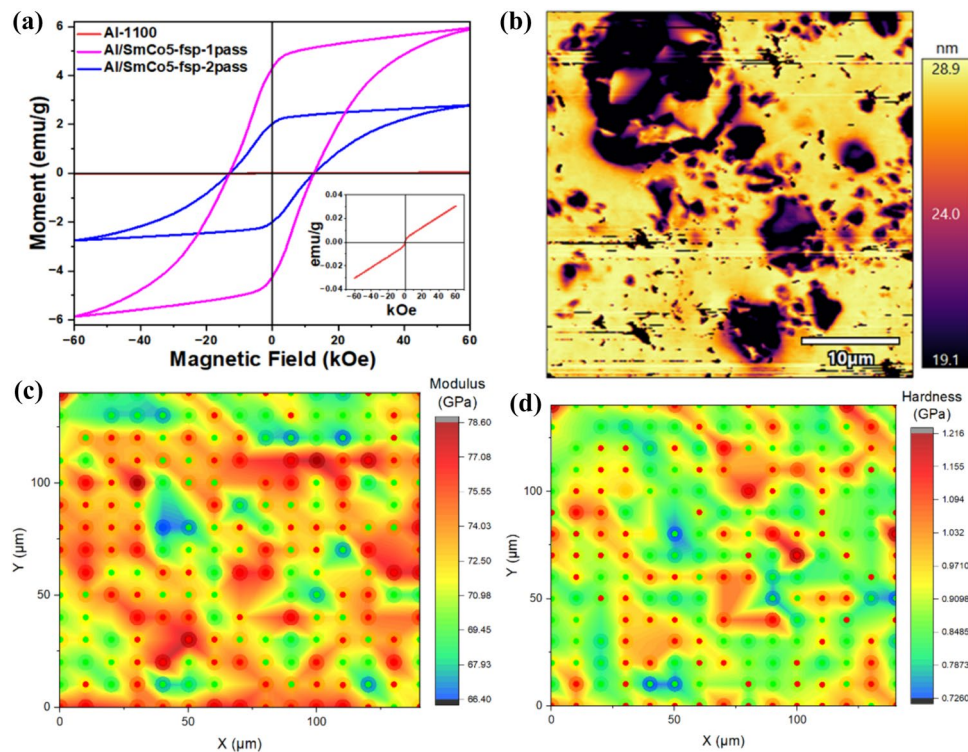


**Figure 3** Bulk magnetic property was assessed by SQUID magnetometry. **a** magnetization ( $M$ ) vs magnetic field ( $H$ ) curves for Al-1100 alloy and same alloy FSPed with magnetic powders; local magnetic response from the same sample was collected using MFM. **b** MFM amplitude map of powder particles in the Al-1100 matrix where the scale bar denotes the signal intensity

of stray field from the composite surface; nanoindentation mapping was conducted with a single cycle load-controlled indentation protocol, where a 6 mN load was applied at 10 μm intervals between total 225 indents. **c** Reduced modulus and **d** hardness map in the FSPed zone using TI-980.



To investigate the effects of the microstructure on the magnetic structure and properties, we performed MFM experiments on the double pass sample. MFM maps sample-tip interaction by sensing cantilever deflection due to stray magnetic fields from the sample. The darker regions in Fig. 3b indicate the presence of a permanent magnetic  $\text{SmCo}_5$  phase inferred by higher bending of the MFM cantilever. Notably, there is no evidence of an interfacial reaction between the matrix and the magnetic particles. This absence of interaction helps preserve the high coercivity of the  $\text{SmCo}_5$  phase in the composite material, as it prevents any magnetic exchange with the matrix that could otherwise lead to domain inversion during demagnetization.

Nanoindentation mapping was conducted on a polished specimen to assess local mechanical property variations within the Al-matrix post-processing with  $\text{SmCo}_5$  particles. Incremental loading helped identify hardness plateaus, with a final load of 6 mN applied in each indent. The resulting reduced modulus and hardness maps are depicted in Fig. 3c and d. The observed increase in mechanical strength can be attributed to the distribution of  $\text{SmCo}_5$  particles in the Al matrix. Modulus and hardness values are divided into two regions (shown in Table 1): the red patches in the nanoindentation maps exhibit higher modulus and hardness values of  $74.6 \pm 1.76$  GPa and  $0.98 \pm 0.08$  GPa, respectively; and the green regions display lower modulus and hardness values of  $70.65 \pm 1.93$  GPa and  $0.86 \pm 0.06$  GPa, respectively. The modulus of elasticity value for Al-1100 alloy was reported to be 68.9 GPa [38]. The increased hardness observed in the FSP-processed sample at specific sites can be attributed to the elevated dislocation density near the  $\text{SmCo}_5$  particles, as well as the inherent hardness of the  $\text{SmCo}_5$  particles themselves [39]. During FSP, the plastic flow of Al around the hard magnetic particles (having a higher modulus) could lead to a higher dislocation density surrounding these particles [40]. Moreover, differential thermal expansion between the magnetic particles and the Al matrix during cooling may also contribute

to this dislocation density. Localized strain field in the matrix induced by the magnetic particles further enhances the hardness in the processed region [31, 41].

To understand the interaction between Al and  $\text{SmCo}_5$  at the nanoscale, a TEM foil was extracted from the top cross section of the processed alloy. In the high-angle-annular-dark-field (HAADF) image (Fig. 4a), grains exhibit an uneven size and shape. Two particles stand out as especially bright in the z-contrast of the HAADF image, both around 500 nm in size and confirmed to be rich in both Sm and Co by EDS, shown in Fig. 4b–e. In combination with the two prior size populations identified in EDS, this confirms that submicron particle sizes can be achieved via shear fracturing in FSP without compromising the magnetic phase. Additionally, a fine-scale Fe-rich phase at the grain boundary, likely due to breakage and/or reprecipitation of the Al-Fe intermetallic phase present in the Al-1100 alloy [42, 43], whereas the refinement of Sm-Co phases results solely from fracture and breakage by stir-induced shear deformation. While Fe is an impurity in the alloy, the typically undesirable  $\text{Al}_{13}\text{Fe}_4$  phases present in the 1100 series can be fragmented and redistributed at a refined scale through FSP. However, it remains unclear whether these phases undergo fragmentation and redistribution or solutionization and reprecipitation under high-speed mechanical stirring. In this study, Al-Fe-rich precipitates were observed on grain boundaries, which could suggest reprecipitation at boundaries or particle-stimulated recrystallization.

Figure 4g–j presents EELS maps for a  $\text{SmCo}_5$  particle depicted in Fig. 4f. The particle displays an elliptical morphology, with an oxygen-rich scale detected at the interface, suggesting either prior oxidation of the  $\text{SmCo}_5$  particles or oxidation during processing. Moreover, the continuity of the interface (without pores) between the Al matrix and the incorporated  $\text{SmCo}_5$  particles indicates excellent adherence, likely enhanced by sufficient material flow during the double-pass FSP. An interfacial reaction between Al and Sm is also visible from the respective maps (yellow

**Table 1** Nanoindentation modulus and hardness from two regions

Statistic	Red region		Green region	
	Young's modulus (GPa)	Hardness (GPa)	Young's modulus (GPa)	Hardness (GPa)
Mean	$74.6 \pm 1.76$	$0.98 \pm 0.08$	$70.65 \pm 1.93$	$0.86 \pm 0.06$
Number of points	98	98	107	107

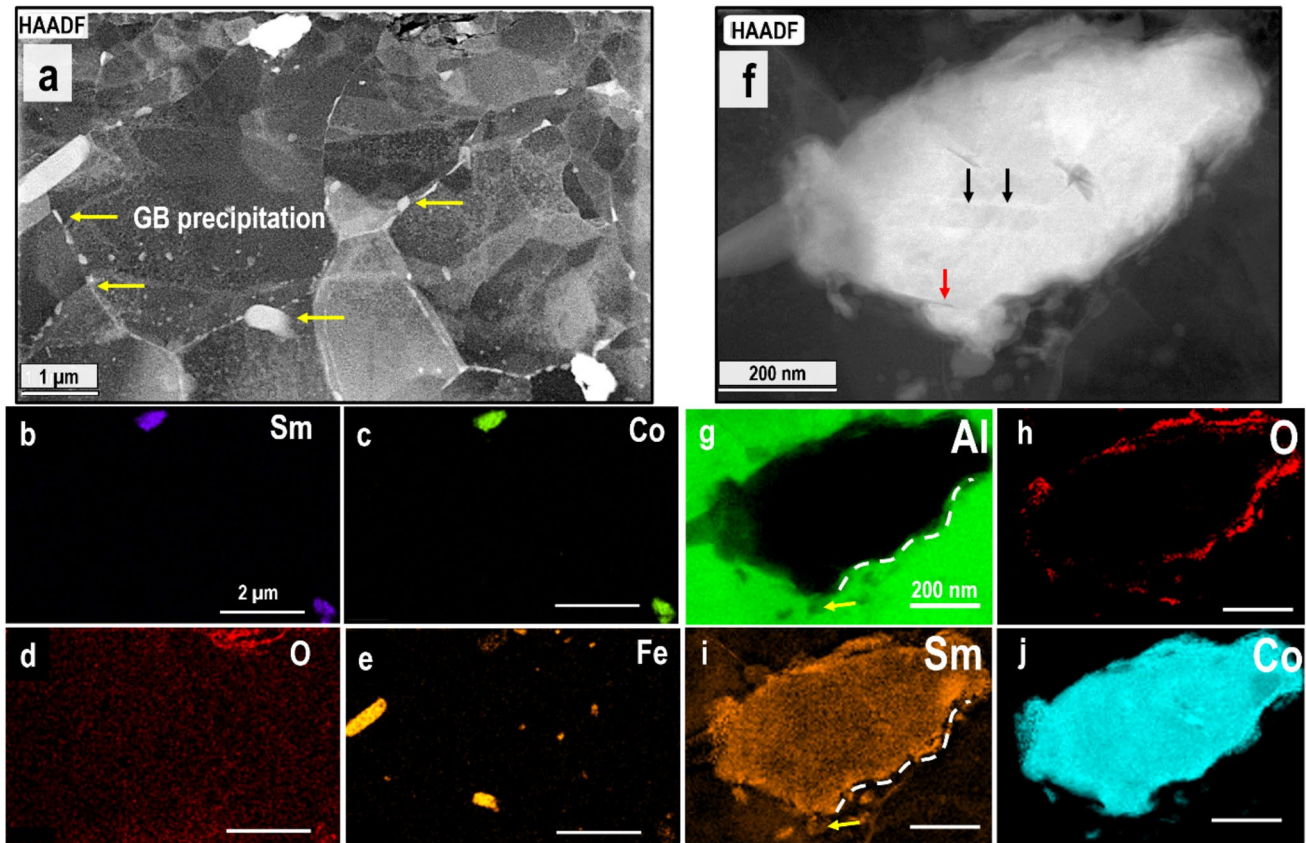


**Figure 4** **a** HAADF STEM image showing two  $\text{SmCo}_5$  particles along with Fe-rich grain boundary (GB) precipitations; **b–e** corresponding EDS signals from Sm, Co, O, and Fe atoms. **f**

HAADF STEM image showing an individual  $\text{SmCo}_5$  particle in the Al-1100 matrix. **g–j** shows elemental maps using EELS.

arrow and dotted line), suggesting the formation of a thin layer of an Al–Sm rich phase due to severe plastic deformation around the particle proving the metallurgical bonding, while keeping the majority of  $\text{SmCo}_5$  phase intact, preserving its magnetic properties. Additionally, evidence of particle fracture along a shear band in  $\text{SmCo}_5$  is observed in Fig. 4f, highlighted with a red arrow indicating crack propagation and the black arrows indicating shear bands within the particle. Prior work from Luo et al. demonstrated the accommodation of plastic deformation within  $\text{SmCo}_5$  grains via thin amorphous shear bands [24], although recent research indicates the formation of dislocations and stacking faults on well-defined crystallographic planes at low deformation rates [44]. The resolution of our findings is limited due to the difficulty in co-milling Al and  $\text{SmCo}_5$  via FIB, though the results suggest the formation of shear bands in the particles due to shear processing.

## Conclusions

In this study, we proposed a shear-based solid-state process to introduce  $\text{SmCo}_5$  permanent magnet particles into an Al-matrix to fabricate a multifunctional metal-bonded magnetic composite. The following conclusions were drawn from the experimental study:

1. Friction stir processing (FSP) was employed to create a surface composite layer on a commercial Al bar, successfully incorporating harder magnetic particles into the softer metal matrix.
2. The intense shear experienced during friction stir processing caused fragmentation of the  $\text{SmCo}_5$  particles, reducing them in size and distributing them heterogeneously within the Al matrix, while adequately suppressing any adverse phase transformations or reactions. X-ray micro- and nanotomography revealed additional passes to

be effective in further reducing particle size and increasing local uniformity and particle density; however, larger-scale heterogeneity of the particle density persisted after 2 passes. TEM revealed that in addition to fragmentation, the  $\text{SmCo}_5$  particles also displayed signs of plastic deformation in the form of shear bands.

3. The Al matrix in the surface composite experienced a significant grain refinement due to a mixture of continuous dynamic recrystallization during processing and particle-stimulated nucleation as a result of the fine distribution of  $\text{SmCo}_5$  particles and the strong adherence of the particles with the matrix.
4. Bulk and local magnetic characterization reveal that the hard magnetic properties of the  $\text{SmCo}_5$  are preserved within the final composite, exhibiting an appreciable coercivity of 13 kOe with the single-pass sample having higher magnetization at zero applied field. The preservation of the coercivity can be attributed in part to the absence of magnetic interaction between the  $\text{SmCo}_5$  particles and the surrounding Al matrix.
5. The mechanical properties of the composite were also improved with the addition of  $\text{SmCo}_5$  particles, with an increase in both the modulus and the hardness of the composite.

This innovative shear-based processing technique holds promise as a tailored solution to produce metal-bonded magnetic composites to meet material requirements in functionalized structural components, offering exciting opportunities for future applications.

## Data and code availability

Data will be available upon request.

## Acknowledgements

The research is supported by ONR under grant N00014-23-1-2758 and was performed at the Center for Additive Manufacturing and Logistics (CAMAL) of North Carolina State University. The microstructural characterization was performed at the Analytical Instrumentation Facility (AIF) at North Carolina State University, which is supported by the State of North Carolina and the National Science Foundation (award

number ECCS-2025064). The AIF is a member of the North Carolina Research Triangle Nanotechnology Network (RTNN), a site in the National Nanotechnology Coordinated Infrastructure (NNCI). The authors acknowledge the Manufacturing Technology Inc. friction stir processing facility available at the Center for Friction Stir Processing (CFSP) at the University of North Texas. The authors are very grateful to Anurag Gumaste at the University of North Texas for helping with the friction-stir experiments. ME acknowledges support from U.S. DOE, Vehicle Technologies Office, through the Powertrain Materials Core Program. Pacific Northwest National Laboratory is operated by Battelle for the U.S. Department of Energy (DOE) under contract DE-AC05-76RL01830.

## Funding

Office of Naval Research Global, N00014-23-1-2758, Bharat Gwalani, National Science Foundation, ECCS-2025064.

## Declarations

**Conflicts of interest** The authors declare no conflicts of interest or competing interests.

**Ethical approval** Not Applicable.

**Supplementary information** Not Applicable.

## References

- [1] Coey JMD (2020) *Engineering* 6:119–131. <https://doi.org/10.1016/j.eng.2018.11.034>
- [2] Coey JMD, Iriyama T (2022) Modern permanent magnets. In: Ormerod J (ed) Croat J. Woodhead Publishing, Cambridge, pp 305–342
- [3] Pallapa M, Yeow JTW (2015) Smart Mater Struct 24:025007–025018. <https://doi.org/10.1088/0964-1726/24/2/025007>
- [4] Benedyk JC (2010) Materials, design and manufacturing for lightweight vehicles. In: Mallick PK (ed) Woodhead Publishing, Cambridge, pp 79–113
- [5] Shin J, Kim T, Kim D, Kim K (2017) *J Alloy Compd* 698:577–590



- [6] Cui J, Roven HJ (2010) *Transact Nonferrous Metals Soc China* 20:2057–2063. [https://doi.org/10.1016/S1003-6326\(09\)60417-9](https://doi.org/10.1016/S1003-6326(09)60417-9)
- [7] Luo C, Qiu X, Su J, Xu Y, Zhao X, Xing F (2021) *J Manuf Processes* 67:487–495. <https://doi.org/10.1016/j.jmapro.2021.05.016>
- [8] Berbon PB, Bingel WH, Mishra RS, Bampton CC, Mahoney MW (2001) *Scripta Mater* 44:61–66. [https://doi.org/10.1016/S1359-6462\(00\)00578-9](https://doi.org/10.1016/S1359-6462(00)00578-9)
- [9] Mishra RS, Ma ZY, Charit I (2003) *Mater Sci Eng: A* 341:307–310. [https://doi.org/10.1016/S0921-5093\(02\)00199-5](https://doi.org/10.1016/S0921-5093(02)00199-5)
- [10] Thomas WM, Nicholas ED, Needham JC, Murch MG, Temple-Smith P, Dawes CJ (1995) Google Patents.
- [11] Rodewald W, Wall B, Katter M, Velicescu M, Schrey P (1993) *J Appl Phys* 73:5899–5901. <https://doi.org/10.1063/1.353515>
- [12] Huang MQ, Zhang LY, Ma BM, Zheng Y, Elbicki JM, Wallace WE, Sankar SG (1991) *J Appl Phys* 70:6027–6029. <https://doi.org/10.1063/1.350082>
- [13] Otani Y, Moukarika A, Sun H, Coey JMD, Devlin E, Harris IR (1991) *J Appl Phys* 69:6735–6737. <https://doi.org/10.1063/1.348900>
- [14] Kelhar L, Zavašnik J, McGuinness P, Kobe S (2016) *J Magn Magn Mater* 419:171–175. <https://doi.org/10.1016/j.jmmm.2016.06.035>
- [15] Brett RL, Rowlinson N, Ashraf MM, Harris IR, Bowen P (1990) *J Appl Phys* 67:4622–4624. <https://doi.org/10.1063/1.344832>
- [16] Chuang S-F, Lee S-L, Lin F-J, Lin J-C (2006) *Powder Metall* 49:328–333. <https://doi.org/10.1179/174329006x128322>
- [17] Ashrafi N, Ariff AHM, Sarraf M, Sulaiman S, Hong TS (2021) *Mater Chem Phys* 258:123895–123908. <https://doi.org/10.1016/j.matchemphys.2020.123895>
- [18] Maleki A, Taherizadeh AR, Issa HK, Niroumand B, Allafchian AR, Ghaei A (2018) *Ceram Int* 44:15079–15085. <https://doi.org/10.1016/j.ceramint.2018.05.141>
- [19] Elsayd A, Shash AY, Mattar H, Löthman PA, Mitwally ME (2023) *Heliyon* 9:e16887–e16897. <https://doi.org/10.1016/j.heliyon.2023.e16887>
- [20] Borgohain C, Acharyya K, Sarma S, Senapati KK, Sarma KC, Phukan P (2013) *J Mater Sci* 48:162–171. <https://doi.org/10.1007/s10853-012-6724-4>
- [21] Mahmoud ERI, Tash MM (2016) *Materials* 9:505–517.
- [22] Bailey G, Orefice M, Sprecher B, Önal MAR, Herraiz E, Dewulf W, Van Acker K (2021) *J Clean Prod* 286:125294–125302. <https://doi.org/10.1016/j.jclepro.2020.125294>
- [23] Samin AJ (2018) *J Nucl Mater* 503:42–55. <https://doi.org/10.1016/j.jnucmat.2018.02.029>
- [24] Luo H, Sheng H, Zhang H, Wang F, Fan J, Du J, Ping Liu J, Szlufarska I (2019) *Nat Commun* 10:3587–3594. <https://doi.org/10.1038/s41467-019-11505-1>
- [25] Zhao Z, Zhao H, Luo H, Liu L, Ding Y, Zhang X, Yao X, Zhang J (2022) *Mater Today Commun* 31:103676–103683. <https://doi.org/10.1016/j.mtcomm.2022.103676>
- [26] Cui B, Liu X, King AH, Ouyang G, Nlebedim CI, Cui J (2020) *Acta Mater* 196:528–538. <https://doi.org/10.1016/j.actamat.2020.06.058>
- [27] Gursoy D, De Carlo F, Xiao X, Jacobsen C (2014) *J Synchrotron Radiat* 21:1188–1193. <https://doi.org/10.1107/S1600577514013939>
- [28] Oliver WC, Pharr GM (1992) *J Mater Res* 7:1564–1583. <https://doi.org/10.1557/JMR.1992.1564>
- [29] P.J.H. W.J. Arbogast, In: *Proceedings of the fifth international conference on trends in welding research*, (Pine Mountain, GA, USA, June 1–5, 1998).
- [30] Escobar J, Gwalani B, Olsza M, Silverstein J, Ajantiwalay T, Overman N, Fu W, Li Y, Bergmann L, Maawad E, Klusemann B, dos Santos JF, Devaraj A (2022) *J Alloy Compd* 928:167007–167015. <https://doi.org/10.1016/j.jallcom.2022.167007>
- [31] Cavaliere P (2005) *Compos Part A: Appl Sci Manuf* 36:1657–1665. <https://doi.org/10.1016/j.compositesa.2005.03.016>
- [32] Malakar A, Suresh KS, Pancholi V, Brokmeier H-G, Schell N (2020) *Mater Charact* 167:110525–110535. <https://doi.org/10.1016/j.matchar.2020.110525>
- [33] Fonda RW, Bingert JF (2007) *Scripta Mater* 57:1052–1055. <https://doi.org/10.1016/j.scriptamat.2007.06.068>
- [34] Escobar J, Silverstein J, Ishrak F, Li L, Soulam A, Li S, Yu A, Mathaudhu S, Ortiz A, Koch C, Devaraj A, Efe M, Gwalani B (2023) *Mater Sci Eng: A* 886:145715. <https://doi.org/10.1016/j.msea.2023.145715>
- [35] Sarkari Khorrami M, Saito N, Miyashita Y, Kondo M (2019) *Mater Sci Eng: A* 744:349–364. <https://doi.org/10.1016/j.msea.2018.12.1>
- [36] Shafiei-Zarghani A, Kashani-Bozorg SF, Zarei-Hanzaki A (2009) *Mater Sci Eng: A* 500:84–91. <https://doi.org/10.1016/j.msea.2008.09.064>
- [37] Chen CH, Knutson SJ, Shen Y, Wheeler RA, Horwath JC, Barnes PN (2011) *Appl Phys Lett* 99:(012504-1)-(012504-3). <https://doi.org/10.1063/1.3607958>
- [38] I. Alloys International, "Aluminum 1100", <https://alloysintl.com/inventory/aluminum-alloys-supplier/aluminum-1100/>. Accessed 04/04 2024.
- [39] Singh RK, Kamat SV, Mathur RP (2015) *J Magn Magn Mater* 379:300–304. <https://doi.org/10.1016/j.jmmm.2014.12.016>

- [40] Ajay Kumar P, Yadav D, Perugu CS, Kailas SV (2017) Mater Des 113:99–108. <https://doi.org/10.1016/j.matdes.2016.09.101>
- [41] Cui GR, Ma ZY, Li SX (2009) Acta Mater 57:5718–5729. <https://doi.org/10.1016/j.actamat.2009.07.065>
- [42] Movahedi M, Kokabi AH, Seyed Reihani SM (2011) Mater Des 32:3143–3149. <https://doi.org/10.1016/j.matdes.2011.02.057>
- [43] Seri O, Furumata K (2002) Mater Corros 53:111–120. [https://doi.org/10.1002/1521-4176\(200202\)53:2](https://doi.org/10.1002/1521-4176(200202)53:2)
- [44] Stollenwerk T, Ulumuddin NZZ, Sun P-L, Lee S-H, Seehaus M, Skokov K, Gutfleisch O, Xie Z, Korte-Kerzel S (2024) Acta Mater 266:119669–119682. <https://doi.org/10.1016/j.actamat.2024.119669>

**Publisher's Note** Springer Nature remains neutral with regard to jurisdictional claims in published maps and institutional affiliations.

Springer Nature or its licensor (e.g. a society or other partner) holds exclusive rights to this article under a publishing agreement with the author(s) or other rightsholder(s); author self-archiving of the accepted manuscript version of this article is solely governed by the terms of such publishing agreement and applicable law.